Hybrid Frequency Pacing for High-Order Transformed Wireless Power Transfer

Wei Liu, *Student Member, IEEE*, K. T. Chau, *Fellow, IEEE*, Christopher H. T. Lee, *Senior Member, IEEE*, Xiaoyang Tian, *Student Member, IEEE*, and Chaoqiang Jiang, *Member, IEEE*

***Abstract*—This paper proposes and implements a hybrid frequency pacing (HFP) technique for resonating a high-order transformed wireless power transfer (WPT) system with robust zero-voltage switching (ZVS). As a hybrid frequency modulation, the proposed HFP can efficiently tune the innate constant-frequency resonances of WPT. It can facilitate the pulse width modulated inverters to totally get rid of the high-frequency hard-switching while reducing the switching frequency and improving the system efficiency. For typical low-order boost-WPT-based scenarios, the rectification effect may cause waveform distortions and involve a very low virtual capacitance, thus leading to great degradations on the ZVS and zero-phase-angle operation. In addition to achieving a load-independent constant-voltage/-current output, a high-order *LCC* network is deeply investigated to act as two-stage impedance transformations. By flexibly utilizing the rectification-caused virtual derivatives with the high-order transformations, it reliably contributes to a robust ZVS-HFP. The experimental system efficiency can be over 91.5% with the full-range ZVS operation. Theoretical analysis and experimental results are both provided to verify the feasibility of proposed ZVS-HFP for tuning the high-order *LCC*-transformed WPT system.**

***Index Terms*—Wireless power transfer, hybrid frequency pacing, high-order *LCC* transformation, zero-voltage switching.**

I. Introduction

As a carrier of wireless energy, the electromagnetic field resonance enables the wireless power transfer (WPT) system to wirelessly deliver wireless power with high efficiency and capacity [1]. Recently, the WPT technology using magnetic resonant coupling [2] is extensively explored and forms the basis of various industrial applications and interdisciplinary areas, such as electric vehicle wireless charging [3], [4], wireless motors [5], wireless lighting [6], wireless energy-on-demand [7] and wireless energy encryption [8]. Identified as an epoch-making technology, the WPT takes the advantages of cleanness and convenience, reliable electrical isolation and maintenance-free over its wired counterparts.

In addition to transferring energy wirelessly, these WPT-based applications desire high controllability of output power, voltage or current. Various control methods were developed, such as for the wireless battery charging [9], wireless motor speed regulation [5] and wireless dimming control [10]. Generally, these control methods can be classified as the pulse width modulation (PWM) [11], [12], pulse density modulation [13], pulse frequency modulation [7], [14], pulse phase or amplitude modulation and hybrid modulation [15]. Also, they can be readily used in either half-bridge or full-bridge inverters. Typically, the PWM involves higher high-frequency hard-switching loss during power control because the zero-voltage-switching (ZVS) operation will be deteriorated by a variable duty cycle without using a complicated ZVS angle control [16]. Although the pulse density modulation can provide the desired ZVS [13], it suffers from the low subharmonics and the need of inverter modification. Similar to the bang-bang/ON-OFF control [17]-[19] modulated near twice the switching frequency, the hybrid frequency pacing (HFP) is regularly modulated between two switching frequencies to directly generate the desired ZVS turning ON-OFF sequence with the shortest modulation period.

To improve the system performance of WPT, the load-independent output characteristics of high-order compensation networks are of increasing interest. First, a double-sided *LCC* compensation network was proposed, which incorporates a ZVS tuning method to enable the WPT system resonating at a constant frequency while keeping independent of the coupling coefficient and load condition [20]. Second, a family of higher-order compensation circuits were identified to exhibit a constant-voltage/-current output with unity power factor and soft-switching [21]. Besides, a general modeling method for arbitrary high-order resonant networks was reported to get both the load-independent voltage and current transfer characteristics [22]. Also, multiple resonant frequencies of high-order resonant networks were developed for the realization of multi-frequency and/or multi-phase WPT [23], [24]. Third, a mixed high-order compensation network was developed for generating multiple constant current outputs for powering light emitting diodes (LEDs) [6]. Withstanding the constraints of transformer parameters, a variable-parameter T-circuit network was demonstrated to merit more design freedom for a flexible charging current/voltage management [9]. Nevertheless, almost all these compensation networks are to improve the output characteristics and to free the system design from constraints. Other important features of the high-order network have not been investigated.

Differing from the general perception that unity power

Manuscript received March 5, 2020; revised May 12, 2020; accepted June 11, 2020. Date of publication ** **, 2020; date of current version ** **, 2020. This work was supported by the Hong Kong Research Grants Council, Hong Kong Special Administrative Region, China under Project 17204317. Recommended for publication by Associate Editor ** **. (*Corresponding author: K. T. Chau.*)

W. Liu, K. T. Chau, and X. Tian are with the Department of Electrical and Electronic Engineering, The University of Hong Kong, Hong Kong. (e-mail: liuwei@eee.hku.hk, ktchau@eee.hku.hk, xytian@eee.hku.hk).

C. H. T. Lee is with the School of Electrical and Electronic Engineering, Nanyang Technological University, Singapore. (e-mail: chtlee@ntu.edu.sg).

C. Jiang is with the Department of Engineering, The University of Cambridge, Cambridge CB2 1TN, U.K. (e-mail: cj426@cam.ac.uk).

factor is desired for WPT systems, a phenomenon of power factor variation was first revealed and studied in both the continuous and discontinuous current modes [25]. For some scenarios such as battery trickle charging and LED dimming, lower power is required in a boost WPT system in which the switching frequency varies around the resonant frequency. During dynamic frequency deviation, the system efficiency and the zero-phase-angle (ZPA) or ZVS operation may fail to maintain. More significantly, the utilization of relevant impedance transformation and caused derivatives is nearly unexplored.

To solve the above problems, a high-order *LCC* network is proposed to act a new role of impedance transformation apart from the conventional compensation for achieving load-independent outputs. This paper conceives a high-order *LCC*-transformed WPT system using an HFP technique that flexibly converts and utilizes the very low rectification-caused impedance and phase derivatives to improve the system performance. It reliably contributes to a robust ZVS without any inverter modification while reducing the switching frequency.

Section II will discuss the operating principle, multiple harmonic analysis and rectification-caused derivatives of the proposed HFP-WPT system. Section III will introduce the two-stage high-order transformations to convert and utilize the caused derivatives. In Section IV, a robust ZVS-HFP technique will be proposed for efficiently tuning the WPT while reducing the switching frequency. In Section V, an experimental prototype will be accordingly constructed and tested to verify the proposed high-order *LCC*-transformed WPT system using the ZVS-HFP technique. A conclusion will be drawn in Section VI.

II. Hybrid Frequency Pacing WPT

A. Topology and Control System

The proposed high-order *LCC*-transformed HFP-WPT system is depicted in Fig. 1. The whole boost WPT system mainly comprises one gallium nitride (GaN) inverter, one series-compensated transmitter and one *LCC*-compensated receiver. The so-called boost WPT works like a boost converter with a step-up ratio. In some WPT-based applications, such as battery trickle charging and LED dimming, their equivalent load resistances may gradually vary to be larger, and thus the system will probably operate at a stage of boost conversion. Consequently, the rectification effect of used rectifiers may cause distortions on the voltage and current, and involve a very low virtual inductance, thus resulting in non-unity power factor and non-ZPA. As an illustration, this paper investigates a research objective of wirelessly powering and dimming multiple LEDs.

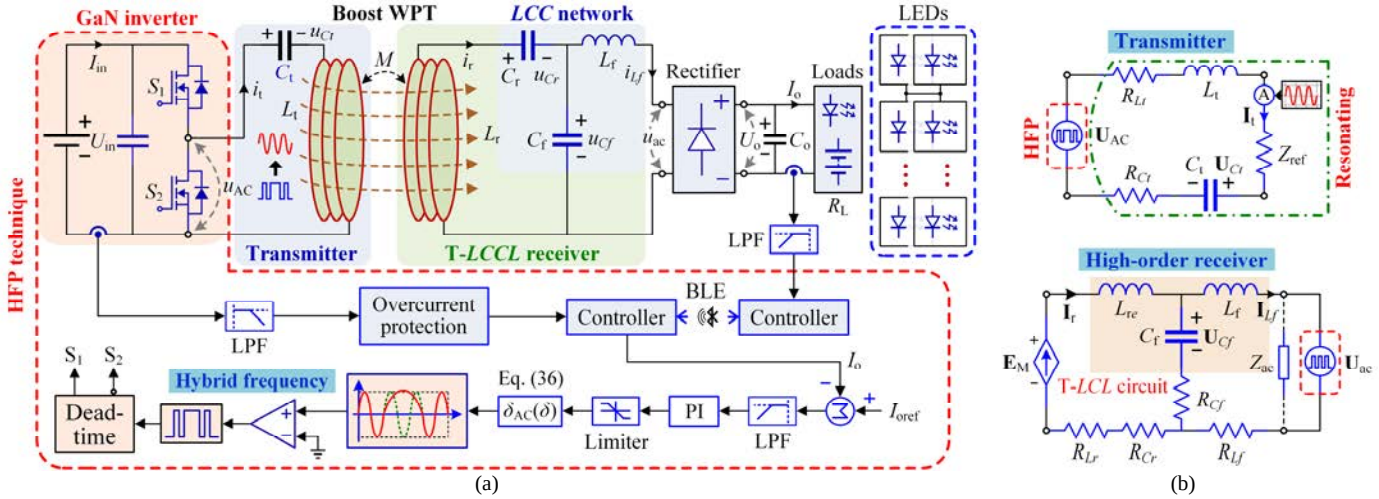

Fig. 1. HFP technique for tuning the high-order *LCC*-transformed boost WPT system. (a) Topology and control. (b) Derived equivalent circuits.

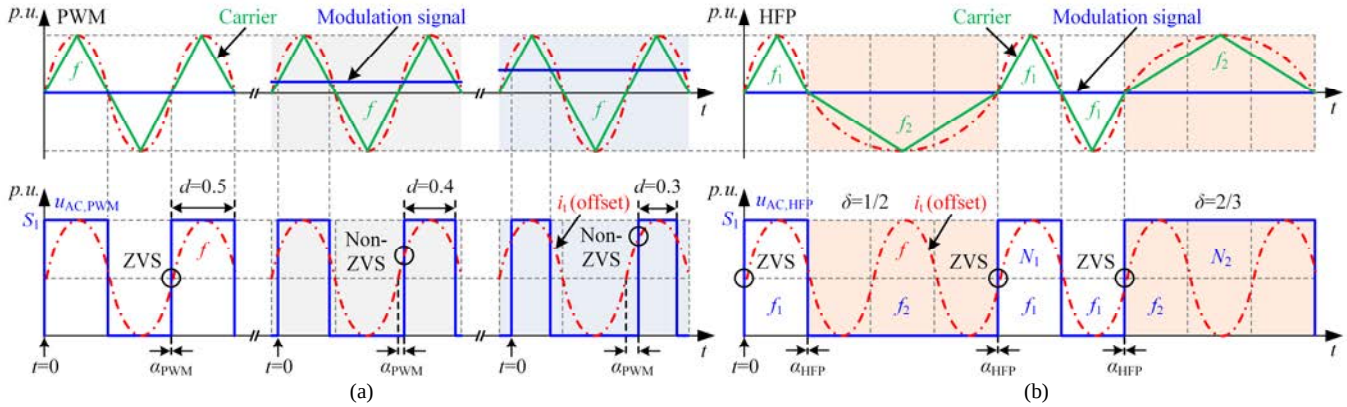

Fig. 2. Alternative pacing control methods with various duty ratios. (a) PWM with non-ZVS. (b) HFP with ZVS.

In Fig. 1, L_t, R_{Lt}, C_t, R_{Ct}, i_t, u_{Ct}, L_r, R_{Lr}, C_r, R_{Cr}, i_r and u_{Cr} with subscripts t and r denote the resonant coil inductances, coil internal resistances, resonant capacitances, capacitor equivalent series resistances (ESRs), resonant currents and

resonant voltages of the transmitter and receiver circuits, respectively; L_f, R_{Lf}, C_f and R_{Cf} are the filter inductor, internal resistance, filter capacitor and ESR; M is the mutual inductance between the WPT coils. The receiver adopts a high-order *LCC* compensation network comprising a filter (L_f, C_f) and a resonant capacitor (C_r), which form a T-*LCCL* (T-type) circuit via directly incorporating with the receiver coil (L_r). Also, the equivalent circuits are derived as shown in Fig. 1(b), where $L_{re}=L_r-1/(\omega^2 C_r)$ is the equivalent inductance. The derived equivalent T-*LCL* WPT scheme can work as one added high-order transformation of the rectification-caused virtual derivatives while additionally contributing to a controllable load-independent constant-voltage/-current output [21], [22] for the WPT-based applications.

Besides, the principle of proposed HFP technique is also illustrated in Fig. 1, where the load current can be sensed at the secondary side with a low-pass filter (LPF), and then remotely delivered to the primary side in real-time via a Bluetooth low energy (BLE) device. Accordingly, a PI controller will be used to regulate the control objective of duty ratio δ. Finally, the HFP sine-wave will be produced for zero-cross comparison and thus generate the driving signals for switching the GaN inverter. Practically, the zero-cross comparison can be implemented in either digital method or analog circuit using an operational amplifier. Also, it can readily be programmed to implement in both the computer simulation and controller. In particular, the PWM interrupt is used to produce the desired HFP gate signal in experimentation. The interrupt frequency is set as twice the resonant frequency ($2f$). When the interrupt count equals N_1 or (N_1+N_2), the interrupt is configured to trigger alternately at the ($2n_f\pm1$)th event, and the gate signal is toggled in the interrupt process, thus directly generating the HFP gate signal. As a result, the HFP technique can readily resonate the proposed high-order *LCC*-transformed WPT system for controlling the illuminance of LEDs remotely at the transmitter side.

To realize the wireless power regulation, the proposed HFP involves two switching frequencies of $f/(2n_f\pm1)$ and modulates them according to a new duty ratio. Usually, the modulated frequencies are selected as the fundamental resonant frequency f and its subharmonic one $f/3$ to satisfy the general requirements. The new duty ratio is a ratio of the fundamental-frequency half-cycle number to the total modulated half-cycle number. Although the HFP is modulated two switching frequencies, it can effectively tune the WPT system with a constant-frequency resonance and achieve the ZVS in the meantime. In particular, two main problems solved can be summarized as follow: First, the proposed HFP technique is to realize the frequency-reduced robust ZVS instead of the non-ZVS under the PWM during power control; Second, the use of high-order transformation is to withstand and tactfully utilize the very low variations of impedance and phase caused by rectification, thus maintaining a robust ZVS. Otherwise, the rectification-caused variations will deteriorate the ZVS by using only a low-order transformation

In conventional WPT schemes, the power regulation usually adopts the PWM control, which is realized by adjusting its duty ratio during each resonant cycle. However, such a variable duty ratio may inevitably cause the high-frequency hard-switching losses and reducing the operation efficiency, thus degrading the system performance. The variable duty ratio of PWM is differed by comparing a variable-amplitude modulation signal with a constant-frequency carrier as shown in Fig. 2(a), whereas that of the proposed HFP is generated by comparing a constant-amplitude modulation signal with a variable-frequency carrier as shown in Fig. 2(b). In contrast, this HFP mechanism can not only suppress the switching frequency but also maintain a full-range robust ZVS against the variable duty ratio and various rectification-caused derivatives owing to the assistance of high-order transformation, thus mitigating the power losses and improving the system efficiency. According to the practical power-on-demand and load characteristics, the proposed HFP technique can be readily extended to apply in various WPT-based applications while maintaining a robust ZVS operation.

B. Multiple Harmonic Analysis of Switching Angle Characteristics

As control objectives in Fig. 2, the duty ratio d of PWM is the pulse width, while the duty ratio $\delta=N_1/(N_1+N_2)$ of HFP is the ratio of the number N_1 of half-cycles, modulated at the frequency of f_1, to the total number (N_1+N_2) of half-cycles, modulated at two frequencies of f_1 and f_2.

Both the PWM and HFP outputs of $u_{AC,PWM}$ and $u_{AC,HFP}$ in Fig. 2 can be expressed in the form of Fourier series

$$u_{AC,PWM}(t,d,\omega)=dU_{in}+\frac{2U_{in}}{n\pi}\sum_{n=1}^{\infty}\sin(n\pi d)\cos\left(n\omega t-\frac{n\omega dT}{2}\right) \tag{1}$$

$$\begin{aligned}u_{AC,HFP}(t,\delta,\omega_1,\omega_2)&=\delta_{DC}U_{in}\\&+\frac{\delta n_1}{\delta n_1+(1-\delta)n_2}\frac{2U_{in}}{n\pi}\sum_{n=1}^{\infty}\sin\left(\frac{n\pi}{2}\right)\cos\left(n\omega_1 t-\frac{n\omega_1 T_1}{4}\right)\\&+\frac{(1-\delta)n_2}{\delta n_1+(1-\delta)n_2}\frac{2U_{in}}{n\pi}\sum_{n=1}^{\infty}\sin\left(\frac{n\pi}{2}\right)\cos\left(n\omega_2 t-\frac{n\omega_2 T_2}{4}\right)\end{aligned} \tag{2}$$

where $u_{AC,HFP}(t, \delta, \omega_1, \omega_2)$ is the average Fourier series of the piecewise HFP output u_{AC}, which contains no even-order harmonics; U_{in} is the DC input voltage; T, T_1 and T_2 are the periods of frequencies f, f_1 and f_2, and ω, ω_1 and ω_2 are their angular frequencies, respectively; $n\in\mathbb{Z}^+$ is the nth harmonic order, and $\delta_{DC}U_{in}$ is the DC component. The n_1th and n_2th terms of trigonometric functions both construct the fundamental component (ω) for tuning the WPT system as given by

$$\begin{aligned}u_{AC,HFP,1}(t,\delta,\omega)=&\\&\frac{\delta n_1}{\delta n_1+(1-\delta)n_2}\frac{2U_{in}}{n_1\pi}\sin\left(\frac{n_1\pi}{2}\right)\cos\left(n_1\omega_1 t-\frac{n_1\omega_1 T_1}{4}\right)\\&+\frac{(1-\delta)n_2}{\delta n_1+(1-\delta)n_2}\frac{2U_{in}}{n_2\pi}\sin\left(\frac{n_2\pi}{2}\right)\cos\left(n_2\omega_2 t-\frac{n_2\omega_2 T_2}{4}\right)\\&=\frac{1}{\delta n_1+(1-\delta)n_2}\frac{2U_{in}}{\pi}\cos\left(\omega t-\frac{n_1\pi}{2}\right)\end{aligned} \tag{3}$$

$$\omega=\underbrace{(2n_f-1)}_{n_1}\omega_1=\underbrace{(2n_f+1)}_{n_2}\omega_2,\ \ n_f\in\mathbb{Z}^+ \tag{4}$$

Thus, the root-mean-square values and ratio coefficients of the nth harmonic PWM and HFP outputs can be generalized as

$$U_{\mathrm{AC,PWM},n}=\frac{\sqrt{2}U_{\mathrm{in}}\sin(n\pi d)}{n\pi},\ \delta_{\mathrm{AC,PWM},n}=\frac{\sin(n\pi d)}{n} \tag{5}$$

$$U_{\mathrm{AC,HFP},n}=\frac{\sqrt{2}U_{\mathrm{in}}/(n\pi)}{\delta n_1+(1-\delta)n_2},\quad \delta_{\mathrm{AC,HFP},n}=\frac{1/n}{\delta n_1+(1-\delta)n_2} \tag{6}$$

Accordingly, these two control methods can be interrelated by $\delta_{\mathrm{AC,HFP},n}=\delta_{\mathrm{AC,PWM},n}$ (n=1, 3, 5, …), where $0<\delta\le 1$ and $0<d\le 50\%$.

In Fig. 2, the switching phase angles of PWM and HFP can be respectively derived as

$$\alpha_{\mathrm{PWM},n,\omega}=\frac{n\pi}{2}-\frac{n\omega dT}{2}=n\pi\left(\frac{1}{2}-d\right) \tag{7}$$

$$\alpha_{\mathrm{HFP},n,\omega_1}=n\left(\frac{\pi}{2}-\frac{\omega_1 T_1}{4}\right)=0^{\mathrm{o}},\ \alpha_{\mathrm{HFP},n,\omega_2}=n\left(\frac{\pi}{2}-\frac{\omega_2 T_2}{4}\right)=0^{\mathrm{o}} \tag{8}$$

Hence, the ZPA can be realized with only d=0.5 under the PWM. Otherwise, it will gradually increase with a decreasing duty ratio d as shown in Fig. 2(a), which indicates that the ZVS will fail and become difficult to maintain against a dynamically varied duty ratio. In contrast, the ZPA can always keep a good tolerance to such a variable duty ratio under the HFP in Fig. 2(b), thus readily realizing and maintaining the ZVS by involving a very low inductance.

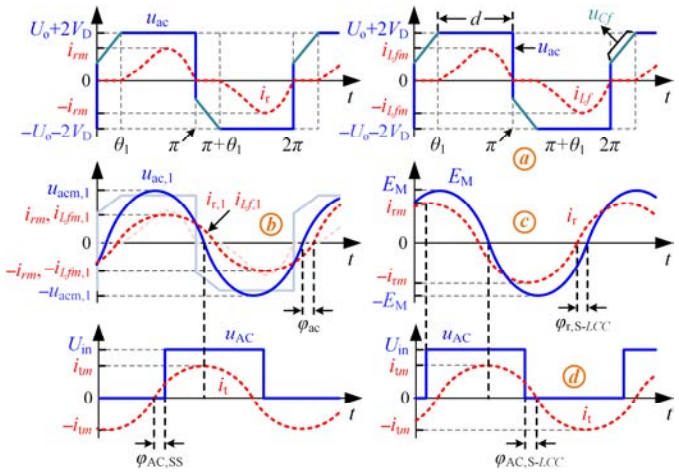

Fig. 3. Theoretical waveforms. (a) SS network. (b) S-*LCC* network (***a***, ***b***, ***c***, ***d***).

C. Rectification-Caused Impedance and Phase Derivatives

In a general WPT system, the rectifier usually works in a continuous current mode. The AC input voltage u_{ac} before the rectification is normally in the shape of a square waveform without DC offset. For a boost WPT system in Fig. 1, however, the existences of rectifier and output filter capacitor C_{o} will result in generating a non-negligible DC voltage source U_{o} after the rectification. Thus, the equivalent circuit of rectification should be regarded as a square-wave voltage source $\mathbf{U}_{\mathrm{ac}}$ rather than a pure load impedance at the secondary side in Fig. 1(b). Worse still, the filter inductor current i_{Lf} and the square-wave voltage u_{ac} will be both distorted (d<0.5) with a highly boost ratio as shown in Fig. 3, where the low-order series-series (SS) and high-order series-*LCC* (S-*LCC*) networks are adopted in Figs. 3(a) and 3(b), respectively. Inevitably, it will cause a series of very low deviations on the impedance, power factor, ZPA operating frequency and switching phase angle, which may slightly change with a varying load, thus deteriorating the ZPA or ZVS operation. The distorted input voltage u_{ac} is rich in harmonics and can be expressed in Fourier series

$$u_{\mathrm{ac}}(t,d,\omega)=\frac{4(U_{\mathrm{o}}+2V_{\mathrm{D}})}{n\pi}\sum_{n=1}^{\infty}\sin\left(\frac{n\pi}{2}\right)\sin(nd\pi)\sin\left[n\omega t-n\left(\frac{1}{2}-d\right)\pi\right] \tag{9}$$

where V_{D} is the diode forward voltage of rectifier.

By applying the multiple harmonic analysis [11], the equivalent impedance can be modeled in the form of vector

$$F(\mathbf{Z}_{\mathrm{ac}})=\begin{bmatrix}Z_{\mathrm{ac},1} & Z_{\mathrm{ac},2} & \cdots & Z_{\mathrm{ac},n}\end{bmatrix}^{\mathrm{T}} \tag{10}$$

All the variables with a subscript n are their nth components. Since the equivalent voltage source in (9) contains no even-order harmonics, the even-order impedances in $\mathbf{Z}_{\mathrm{ac}}$, such as $Z_{\mathrm{ac},2}$ or $Z_{\mathrm{ac},4}$, can be ignored. The filter current vector comprising the fundamental and harmonic components can be expressed as

$$F(\mathbf{I}_{Lf})=\begin{bmatrix}\mathbf{I}_{Lf,1} & \mathbf{I}_{Lf,2} & \cdots & \mathbf{I}_{Lf,n}\end{bmatrix}^{\mathrm{T}} \tag{11}$$

where each element can be accordingly derived as

$$i_{Lf,n}(t)=\frac{u_{\mathrm{ac},n}(t)}{Z_{\mathrm{ac},n}}=\frac{4(U_{\mathrm{o}}+2V_{\mathrm{D}})}{Z_{\mathrm{ac},n}n\pi}\sin\left(\frac{n\pi}{2}\right)\sin(nd\pi)\sin\left[n\omega t-n\left(\frac{1}{2}-d\right)\pi\right] \tag{12}$$

In Fig. 1(b), assuming $R_{\mathrm{t}}=R_{Lt}+R_{Ct}$, $R_{\mathrm{r}}=R_{Lr}+R_{Cr}$, and $R_{\mathrm{f}}=R_{Lf}+R_{Cf}$, the Kirchhoff's voltage law provides the general equation as given by

$$\begin{bmatrix}-\mathbf{U}_{\mathrm{ac},n}\\ \mathbf{E}_{\mathrm{M},n}\end{bmatrix}=\begin{bmatrix}R_{Lf}+Z_{Lf,n}+Z_{Cf,n} & -Z_{Cf,n}\\ -Z_{Cf,n} & R_{\mathrm{r}}+Z_{Lre,n}+Z_{Cf,n}\end{bmatrix}\begin{bmatrix}\mathbf{I}_{Lf,n}\\ \mathbf{I}_{\mathrm{r},n}\end{bmatrix} \tag{13}$$

where $Z_{Lre,n}=jn\omega L_{\mathrm{re}}$, $Z_{Cf,n}=1/(jn\omega C_{\mathrm{f}})+R_{Cf}$, and $Z_{Lf,n}=jn\omega L_{\mathrm{f}}$. It yields

$$Z_{\mathrm{ac},n}=\frac{-\mathbf{U}_{\mathrm{ac},n}}{\mathbf{I}_{Lf,n}}=R_{Lf}+Z_{Lf,n}+Z_{Cf,n}-\frac{Z_{Cf,n}^2}{R_{\mathrm{r}}+Z_{Lre,n}+Z_{Cf,n}}-\frac{Z_{Cf,n}}{R_{\mathrm{r}}+Z_{Lre,n}+Z_{Cf,n}}\frac{\mathbf{E}_{\mathrm{M},n}}{\mathbf{I}_{Lf,n}} \tag{14}$$

$$\frac{\mathbf{E}_{\mathrm{M},1}}{\mathbf{I}_{Lf,1}}=\frac{(R_{\mathrm{r}}+R_{Cf})\left[R_{\mathrm{f}}+\Re(Z_{\mathrm{ac},1})\right]}{Z_{Cf,1}}-Z_{Cf,1} \tag{15}$$

Defining $\boldsymbol{\omega}=[\omega\ 2\omega\ 3\omega\ \cdots\ n\omega]$, the phasors of the induced electromotive force $\mathbf{E}_{\mathrm{M}}=j\boldsymbol{\omega}M\mathbf{I}_{\mathrm{t}}$ and the transmitter current $\mathbf{I}_{\mathrm{t}}$ dominantly comprise the fundamental components nearly without the high-order harmonics. Also, the fundamental impedance $Z_{\mathrm{ac},1}$ and the high-order harmonic one $Z_{\mathrm{ac},n}$ (n>1) can be respectively derived as

$$Z_{\mathrm{ac},1}=\frac{-\mathbf{U}_{\mathrm{ac},1}}{\mathbf{I}_{Lf,1}}=R_{\mathrm{f}}-\frac{Z_{Cf,1}}{R_{\mathrm{r}}+R_{Cf}}\left(Z_{Cf,1}+\frac{\mathbf{E}_{\mathrm{M},1}}{\mathbf{I}_{Lf,1}}\right)=\Re(Z_{\mathrm{ac},1}) \tag{16}$$

$$Z_{\mathrm{ac},n}=\frac{-\mathbf{U}_{\mathrm{ac},n}}{\mathbf{I}_{Lf,n}}=R_{Lf}+Z_{Lf,n}+Z_{Cf,n}-\frac{Z_{Cf,n}^2}{R_{\mathrm{r}}+Z_{Lre,n}+Z_{Cf,n}} \tag{17}$$

Finally, the rectification circuit can be expressed by its equivalent complex impedance as

$$Z_{\mathrm{ac}}=F(\mathbf{Z}_{\mathrm{ac}})^{\mathrm{T}}F(\mathbf{I}_{Lf})\frac{Z_{\mathrm{ac},1}}{U_{\mathrm{ac},1}}=\Re(Z_{\mathrm{ac}})+j\Im(Z_{\mathrm{ac}}) \tag{18}$$

where $\Re(\cdot)$ and $\Im(\cdot)$ denote the real part and the imaginary part, respectively. The phase φ_{ac}, by which $\mathbf{U}_{ac}$ leads $\mathbf{I}_{Lf}$, is close to zero ($0^o<\varphi_{ac}\ll 90^o$) and can be obtained as

$$\varphi_{ac} = \arctan\left(\frac{\Im(Z_{ac})}{\Re(Z_{ac})}\right) \tag{19}$$

Since the amplitudes of high-order harmonics decrease to be extremely low, φ_{ac} can be accurately predicted by choosing a proper value of n. With a series of very low derivatives, the operating frequency of inverter may need to slightly deviate for maintaining the ZPA or ZVS operation. However, such derivatives may be sensitively influenced by the changes in load and displacements.

D. Scenario of Removing DC Filter Capacitor

Providing that the DC filter capacitor C_o after the rectifier is removed, the AC input voltage u_{ac} is rectified to become the positive sinusoidal half-cycles, and the rectified DC output voltage U_o will freewheel without filtering. Hence, the rectification will no longer generate a constant DC voltage source U_o. The rectifier will work in a continuous current mode again just like in a general WPT system with a unity power factor, and thus its input voltage and current are both theoretically sinusoidal without any distortions. The equivalent circuit of rectifier can be modeled as a pure load impedance instead of a square-wave voltage source $\mathbf{U}_{ac}$ in Fig. 1(b). Consequently, the phenomena of waveform distortions as well as the rectification-caused impedance and phase deviations will disappear once removing the filter C_o.

III. High-Order Impedance Transformation

A. One-Stage Transformation with Low-Order Compensation

The system characteristics are dominated by the fundamental components of variables, and thus the first harmonic analysis can still be used as an effective study on the transformation of caused impedance and phase derivatives. In Fig. 4, instead of connecting $C_{r,P}$ in parallel, the SS topology concatenates $C_{r,S}$ in series. Since the series-parallel topology suffers from high sensitivity of displacement deviations and load variations, the SS one is selected as the research objective for comparative analysis. To tune the SS-WPT resonance, its resonant parameters should satisfy $L_tC_t=L_rC_{r,S}=1/\omega^2$.

Representing the virtual inductor $-M$ by an equivalent capacitor C_M [6], their values can be equivalently interrelated as

$$C_M = \frac{1}{\omega^2 M} \tag{20}$$

With the SS compensation, the process of one-stage impedance transformation among the ports *1-4* in Fig. 4 can be written as

$$Z_{12,SS} = j\omega L_r + \frac{1}{j\omega C_r} + R_r + Z_{ac} \tag{21}$$

$$Z_{34,SS} = \frac{(\omega M)^2\left[R_r + \Re(Z_{ac}) - j\Im(Z_{ac})\right]}{\left[R_r + \Re(Z_{ac})\right]^2 + \Im(Z_{ac})^2} \tag{22}$$

$$Z_{AC,SS} = j\omega L_t + \frac{1}{j\omega C_t} + R_t + Z_{34,SS} \tag{23}$$

where $Z_{AC,SS}$ denotes the input impedance of transmitter. Accordingly, the very low inductance $\Im(Z_{ac})$ will be converted into a capacitance $\Im(Z_{34,SS})$ at the primary said. Fig. 5 shows the theoretical phasor diagram, which well agrees with the analysis of SS network in Fig. 3. Considering no parasitic resistances of resonant circuits, the rectification-caused inductive impedance angle φ_{ac} will be delivered as a same capacitive impedance angle ($\varphi_{AC}=\varphi_{ac}$) to the primary said, while $\varphi_{AC}<\varphi_{ac}$ once taking into account the parasitic resistances. Because of failing to utilize the rectification-caused impedance, the input voltage $\mathbf{U}_{AC}$ lags the transmitter current $\mathbf{I}_t$ by a very small angle, which deteriorates the ZPA or ZVS operation unless dynamically deviating the initial frequency under both the PWM and HFP.

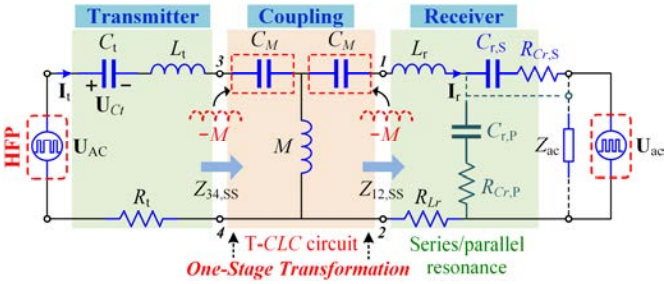

Fig. 4. Simplified equivalent circuit with low-order compensation.

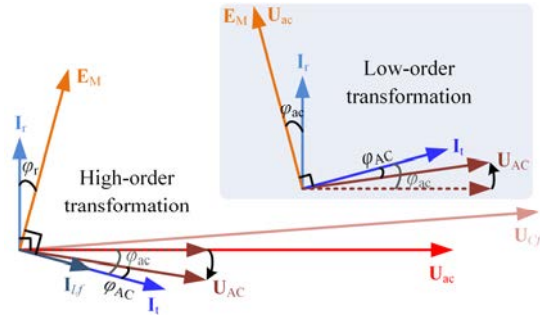

Fig. 5. Theoretical phasor diagrams.

B. Two-Stage Transformation with High-Order Compensation

With the high-order *S-LCC* compensation, the resonant parameters should be tuned as

$$\begin{cases} L_t \cdot C_t = \dfrac{1}{\omega^2}, \quad L_f \cdot C_f = \dfrac{1}{\omega^2} \\ L_r - L_f = \dfrac{1}{\omega^2 C_r}, \quad L_{re} = L_f = L_r - \dfrac{1}{\omega^2 C_r}, \quad L_{re} \cdot C_f = \dfrac{1}{\omega^2} \end{cases} \tag{24}$$

In Fig. 6, the first-stage impedance transformation happens via the T-*LCL* circuit to the ports *1-2* as given by

$$Z_{12,S\text{-}LCC} = R_r + R_{Cf} - \frac{\left(j\omega L_f - R_{Cf}\right)^2}{R_f + \Re(Z_{ac}) + j\Im(Z_{ac})} = R_r + R_{Cf} - \frac{B - jC}{A} \tag{25}$$

$$A = \left[R_f + \Re(Z_{ac})\right]^2 + \Im(Z_{ac})^2 \tag{26}$$

$$B = \left[R_{Cf}^2 - (\omega L_f)^2\right]\left[R_f + \Re(Z_{ac})\right] - 2\omega L_f R_{Cf}\Im(Z_{ac}) \tag{27}$$

$$C = \Im(Z_{ac})\left[R_{Cf}^2 - (\omega L_f)^2\right] + 2\omega L_f R_{Cf}\left[R_f + \Re(Z_{ac})\right] \tag{28}$$

which converts the very low inductance $\Im(Z_{ac})$ to become a very low capacitance $\Im(Z_{12,S\text{-}LCC})$. In Fig. 5, the phase φ_{ac}, by which $\mathbf{U}_{ac}$ leads $\mathbf{I}_{Lf}$, is transformed as a phase φ_r, by which $\mathbf{E}_M$

lags $\mathbf{I}_r$.

The second-stage transformation is realized by the T-*CLC* circuit to the ports *3-4*. Such a capacitance $\Im(Z_{12,S\text{-}LCC})$ will be converted into a very low inductance $\Im(Z_{34,S\text{-}LCC})$ as given by

$$Z_{34,S\text{-}LCC}=\frac{A(\omega M)^2\left\{A\left(R_r+R_{Cf}\right)-B-jC\right\}}{\left[A\left(R_r+R_{Cf}\right)-B\right]^2+C^2} \tag{29}$$

The input impedance of $Z_{AC,S\text{-}LCC}$ has the same form with $Z_{AC,SS}$ in (23). In Fig. 5, the phase φ_r is further transformed as a phase φ_{AC}, by which $\mathbf{U}_{AC}$ leads $\mathbf{I}_t$, which well agrees with the analysis of high-order S-*LCC* network in Fig. 3. It is close to zero ($0^o<\varphi_{AC}\ll 90^o$) and can be slightly reduced as given by

$$\varphi_{AC}=\arctan\left[\frac{-C}{A\left(R_r+R_{Cf}\right)-B}\right]<\varphi_{ac} \tag{30}$$

The introduction of a high-order *LCC*-compensated network adds an extra stage of impedance transformation. Consequently, the very low rectification-caused inductance $\Im(Z_{ac})$ can be indirectly delivered to the primary side for contributing to a ZVS. Taking into account the parasitic resistances of high-order networks, the introduced high-order transformation can slightly suppress a series of tiny rectification-caused deviations on the impedance, power factor, ZPA operating frequency and switching phase angle. Finally, it succeeds to flexibly utilize the caused derivatives and leads the rectifier input impedance Z_{ac} to be transformed as a tinier transmitter input inductance $Z_{AC,S\text{-}LCC}$ for the robust ZVS realization.

With the two-stage transformations of two T-type circuits, the transmitter current phasor $\mathbf{I}_t$ and the receiver filter one $\mathbf{I}_{Lf}$ are in phase. From (6) and (9), the fundamental component of input voltage $u_{AC,HFP}$ at the primary side can be rewritten as

$$u_{AC,HFP,1}(t,\delta,\omega)=\frac{2U_{in}/\pi}{\delta N_1+(1-\delta)N_2}\sin\left[\omega t-\left(\frac{1}{2}-d\right)\pi-\left(\varphi_{ac}-\varphi_{AC}\right)\right] \tag{31}$$

For the exemplified scenarios of battery trickle charging and LED dimming, the load may continuously vary during power control, thus inevitably leading to a variable impedance phase φ_{AC}. In the boost WPT systems with probably varying loads, a coefficient ΔC_t is designed to optimize the capacitor C_t and to compensate the rectification-caused inductance as given by

$$\min\left(\Im\left(Z_{AC}\right)\right)+\omega L_t-\frac{1}{\omega\left(C_t-\Delta C_t\right)}<\varepsilon \tag{32}$$

where ε is a minimal positive number. Thus, a very low inductance can be properly remained for realizing and maintaining the ZVS under the HFP rather than the PWM due to its variable duty ratio *d*.

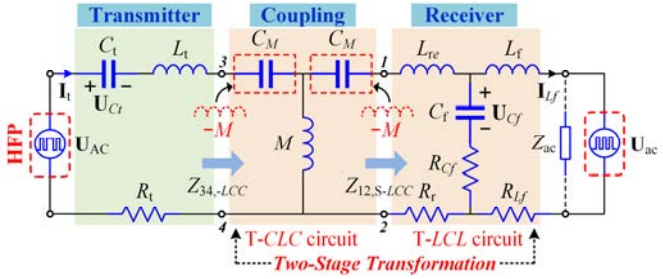

Fig. 6. Simplified equivalent circuit with high-order compensation.

C. Frequency-Domain Analysis

In Fig. 3, the rectification may cause a low inductance in the output impedance Z_{ac}. System optimization is not conducted by either optimizing C_t or slightly reducing the switching frequency. No matter in Fig. 7 or in Fig. 8, without the rectification-caused derivatives of impedance and phase, the ZPA operation can be realized in both the low-order and high-order transformations, while the ZPA operation will happen slight deviations once considering the rectification-caused derivatives. Since the rectification-caused impedance and phase derivatives are very low, the slight non-ZPA operation can be tolerated at the receiver side. Significantly, the rectification-caused derivatives may be sensitively influenced by the changes in load and displacements. It is difficult to be completely compensated but ready to be utilized by involving the high-order transformation for the ZVS-HFP.

However, the one-stage low-order transformation forms only one T-*CLC* circuit as shown in Fig. 4. In Fig. 7, this low rectification-caused inductive impedance will be transformed as a variably capacitive impedance, which will lead to a failed utilization of rectification-caused derivatives. Consequently, the ZVS will be deteriorated even by using either the proposed HFP or the PWM. In contrast, the two-stage high-order transformation can form two T-circuits as shown in Fig. 6. In Fig. 8(a), the first T-*LCL* circuit can transform the rectification-caused inductive impedance to a low capacitive impedance. In Fig. 8(b), the second T-*CLC* circuit can further transform the generated capacitive impedance to a low inductive impedance again. Also, either optimizing C_t or slightly reducing the switching frequency can compensate the rectification-caused variations, and thus the phase angle $\varphi_{AC,S\text{-}LCC}$ is reduced to a proper one which facilitates the proposed HFP to maintain a robust ZVS during power control.

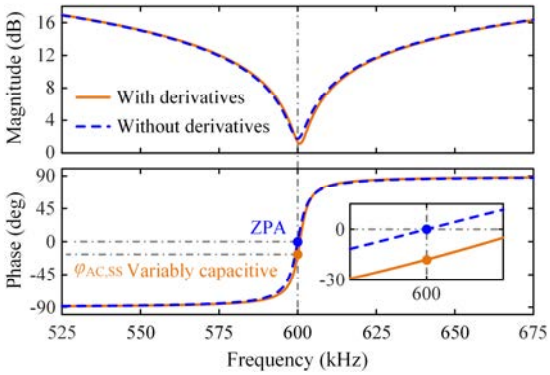

Fig. 7. Input impedance characteristics with low-order transformation.

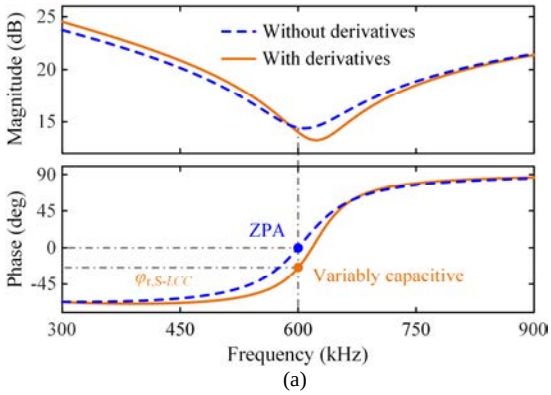

(a)

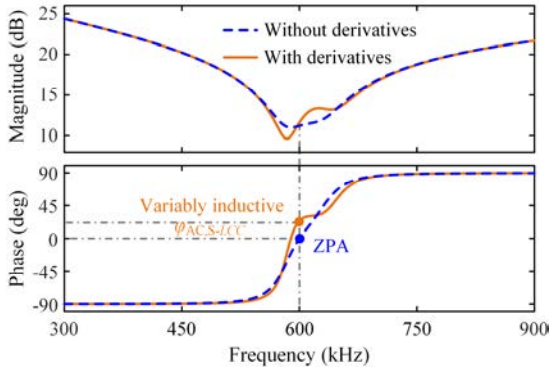

(b)

Fig. 8. Impedance characteristics with high-order transformation. (a) Receiver impedance (first transformation). (b) Input impedance (second transformation).

IV. Hybrid Frequency Pacing Technique

A. Invariance of Oscillation Frequency

According to the equivalent circuits in Fig. 1(b), the reflected impedance can be written as $Z_{\text{ref}}=Z_{34,\text{S-}LCC}$. The operating parameters of transmitter can be expressed in the complex frequency domain as

$$\begin{cases} I_{\text{t}}(s)=\dfrac{\left(U_{\text{in}}/s-U_{Ct}(0\_)/s\right)}{\Re\left(Z_{34,\text{S-}LCC}\right)+R_{\text{t}}+sL_{te}+1/C_{\text{t}}s} \\ U_{Ct}(s)=\left[\dfrac{U_{\text{in}}}{s}-\dfrac{U_{Ct}(0\_)}{s}\right]\dfrac{1/C_{\text{t}}s}{\Re\left(Z_{34,\text{S-}LCC}\right)+R_{\text{t}}+sL_{te}+1/C_{\text{t}}s} \end{cases} \tag{33}$$

where $s=\sigma+j\omega$ is a complex frequency parameter with a real number σ; $L_{te}=L_{\text{t}}+\Im(Z_{34,\text{S-}LCC})/\omega$, and $U_{Ct}(0\_)$ is the initial voltage through C_{t} at the beginning of each switching period. By applying the inverse Laplace transform, (33) can be solved as

$$\begin{cases} i_{\text{t}}(t)=\dfrac{U_{\text{in}}-U_{Ct}(0\_)}{\omega L_{\text{t}}}e^{-\alpha t}\sin\left(\sqrt{1-(\alpha/\omega)^2}\,\omega t\right) \\ u_{Ct}(t)=\left[U_{\text{in}}-\left[U_{\text{in}}-U_{Ct}(0\_)\right]e^{-\alpha t}\cos\left(\sqrt{1-(\alpha/\omega)^2}\,\omega t\right)\right] \end{cases} \tag{34}$$

where

$$\alpha=\frac{\Re\left(Z_{34,\text{S-}LCC}\right)+R_{\text{t}}}{2\left[L_{\text{t}}+\Im\left(Z_{34,\text{S-}LCC}\right)/\omega\right]} \tag{35}$$

TABLE I
Proposed HFP Examples for Tuning WPT

Duty ratio δ	Period T_{HFP}	HFP voltage u_{AC} and resonant i_{t}	Output ratio $\delta_{\text{AC,HFP,1}}$
1	T		1
1/2	$2T$		1/2
1/3	$7T$		3/7
2/3	$5T$		3/5
1/4	$5T$		2/5
3/4	$3T$		2/3

The frequency deviation factor $\sqrt{1-(\alpha/\omega)^2}$ is nearly unity because of $(\alpha/\omega)^2\simeq 0\ll 1$. The transmitter resonant angular frequency can be further expressed as $\omega_{\text{t}}=\omega\sqrt{1-(\alpha/\omega)^2}\simeq\omega$. Thus, the system oscillation frequency is identified to retain approximately constant in the boost WPT resonated by the HFP technique. This oscillation frequency invariance contributes to the realization of robust ZVS-HFP modulated between two optimal frequencies of $f/(2n_f\pm1)$ regularly. Although the amplitude of transmitter current might suffer from slight exponential decays, the WPT resonances can still be tuned by the HFP strategy and exhibit a good tolerance to such exponential decays.

B. Zero-Voltage Switching and Switching Frequency Reduction

Two alternative pacing control methods – the PWM and the proposed HFP are illustrated in Fig. 2 for power adjustment. Both Fig. 2(a) and (7) indicate that the PWM will involve an increasing switching phase angle with a decreasing duty ratio d, and thus the ZVS cannot be readily guaranteed against such a variable duty ratio, especially with only fixed compensations. To add insult to injury, the hard-switching PWM inverter will operate at a constant high frequency. The deteriorated high-frequency hard-switching will result in more power losses and thus inevitable degradations of the system performance.

In contrast, with different duty ratios δ, the proposed HFP can successfully stimulate the *LCC*-transformed WPT to work at a constant-frequency resonance as shown in Fig. 2(b), where two hybrid switching frequencies of f_1 and f_2 are chosen and regularly modulated at $f/(2n_f\pm1)$ ($n\in\mathbb{Z}^+$). By controlling the duty ratio δ between two hybrid modulated frequencies, the load current I_{o} in Fig. 1(a) can be accurately predicted by

$$I_{\text{o}}=\delta_{\text{AC,HFP,1}}I_{\text{orate}}=\frac{I_{\text{orate}}}{\delta n_1+(1-\delta)n_2} \tag{36}$$

where I_{orate} is the rated load current when δ=1. The duty ratio δ of HFP can be derived as

$$\delta=\frac{N_1}{N_1+N_2}=\frac{\left(2n_f+1\right)-1/\delta_{\text{AC,HFP,1}}}{2},\ (N_1,\ N_2\in\mathbb{N}) \tag{37}$$

where N_1 and N_2 denote the minimum modulated numbers of half-cycles switching at f_1 and f_2, respectively. Under the HFP, minimizing the numbers N_1 and N_2 can enable to lower the input fluctuations and thus the output ones for system optimization.

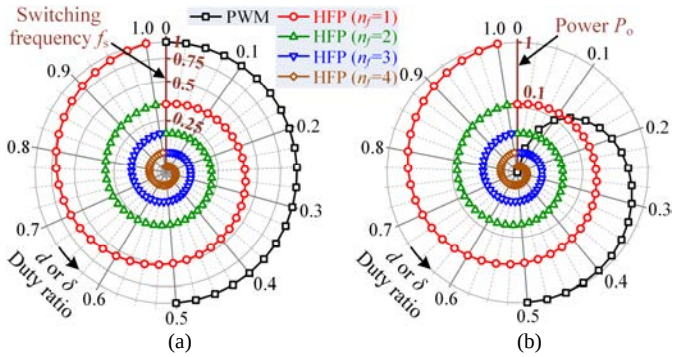

(a) (b)

Fig. 9. Control characteristics versus duty ratios d (PWM) and δ (HFP). (a) Normalized average switching frequency f_s. (b) Normalized wireless power P_o.

For tuning the innate constant-frequency resonance of various WPT systems, some HFP examples are listed in Table I for illustration. As indicated in Fig. 2(b) and (8), the HFP can maintain a stable switching phase angle for the ZVS which is capable of withstanding the varying duty ratio and also satisfying the requirement of power control. By introducing the two-stage high-order impedance transformations, the converted tiny inductance in $Z_{AC,S\text{-}LCC}$ will contribute to the full-range ZVS operation during power control with only fixed compensations. Significantly, the ZVS-HFP can promisingly reduce both the high hard-switching frequency and power losses suffered by the PWM, thus improving the system efficiency.

To demonstrate their control characteristics, Figs. 9(a) and 9(b) show the normalized switching frequency f_s and the wireless power P_o with respective to the duty ratios d ($0<d\leq 0.5$) in the PWM and δ ($0<\delta\leq 1$) in the HFP, respectively, where $\delta_{AC,PWM,1}=\delta_{AC,HFP,1}$ according to (5) and (6). Fig. 9(a) indicates that the average switching frequency of proposed HFP technique presents a reciprocal spiral which is the inverse of Archimedes spiral. Under the HFP, the average switching frequency f_s will monotonously reduce with the decreasing δ and n_f during power control. Instead of switching at a constant high frequency, using the HFP can effectively reduce the average switching frequency as compared with using the PWM. Fig. 9(b) shows a visualized comparison of the power control performance, both wireless powers P_o exhibit monotonously increases with the increasing d and δ or the decreasing n_f under the two above control methods. Also, the HFP can output 11.11% (or 4.0%) of the rated power with n_f =1 (or 2) when δ=0 according to (6), which can sufficiently meet the needs of power control.

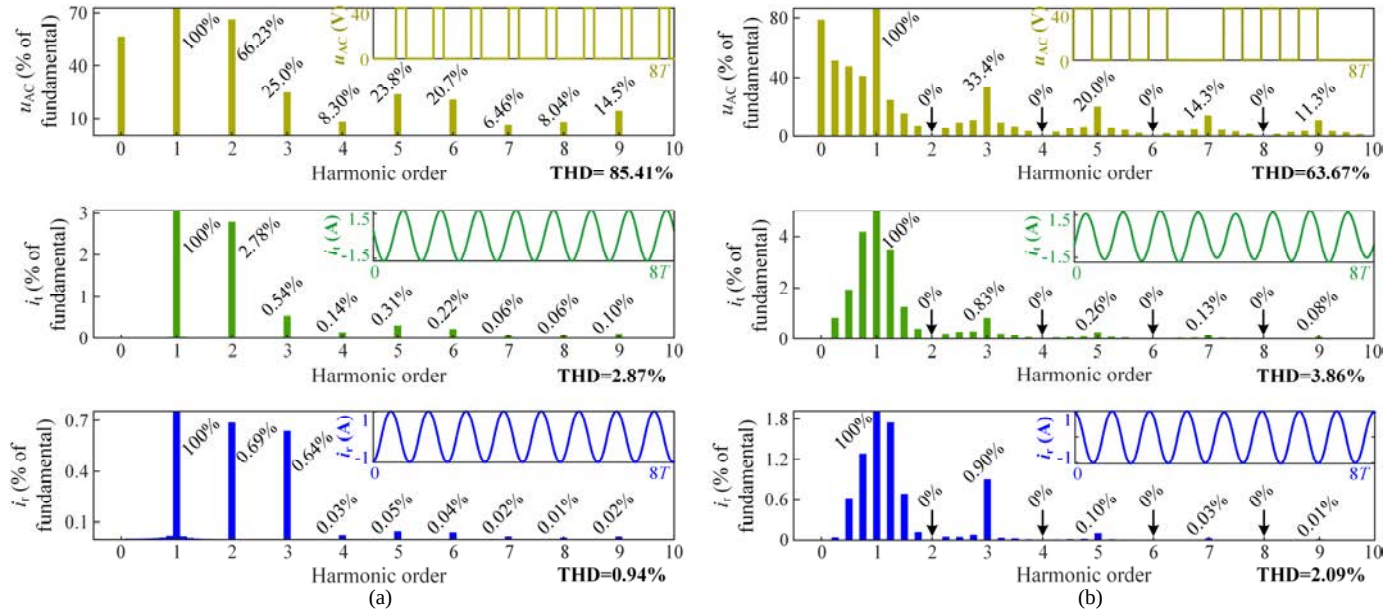

Fig. 10. Harmonic spectrums using FFT analysis. (a) PWM (d=0.27). (b) HFP (δ=5/6).

C. Harmonic Analysis

By using the fast Fourier transformation (FFT), Figs. 10(a) and 10(b) show the harmonic spectrums of the inverter output u_{AC}, transmitter current i_t and receiver current i_r at a 400-Ω load under the PWM and the HFP, respectively. In Fig. 10(a), the total harmonic distortions (THDs) of u_{AC}, i_t and i_r are 85.41%, 2.87% and 0.94%, respectively. Since the PWM duty cycle d=0.27 is lower than 0.5, the even-order (2^{nd}, 4^{th}, 6^{th}, …) harmonic components are produced and considerable, thereby degrading the THD performance, especially for u_{AC}. In Fig. 10(b), the HFP duty ratio δ=5/6 is to equivalently control the fundamental of u_{AC}. By eliminating the even-order harmonics, the HFP can effectively reduce the THD of u_{AC} to 63.67% at the expense of slightly increasing the inter-harmonics and subharmonics. The high-order (3^{rd}, 5^{th}, 7^{th}, …) harmonics, inter-harmonics and subharmonics are all significantly suppressed by the WPT resonant circuits. Hence, the THDs of i_t and i_r are 3.86% and 2.09%, slightly higher than those under the PWM by around only 1%, which is mainly due to the inter-harmonics and subharmonics near the switching frequency. Nevertheless, the HFP can realize a robust ZVS for power control.

D. Phase Characteristics and Efficiency Against Deviations

Without system optimizations by optimizing capacitor and deviating frequency, Fig. 11 quantitatively assesses the caused influences on phase characteristics with respect to the varying loads and mutual inductances, respectively, after adding only a high-order *LCC*-transformation. In Fig. 11(a), with a 5.0-μH mutual inductance, neither the virtual impedance nor the phase derivative occurs without using rectifier or filter capacitor C_o. Otherwise, they will gradually rise to a steady top value with the increasing loads when the WPT operates at a boost mode. In the high-order *LCC*-transformed WPT, the phases φ_{AC} and φ_{ac} are both positive values as a result of the high-order transformation. Also, φ_{AC} is slightly lower than φ_{ac} due to the parasitic resistances. With the varying mutual inductances caused by displacement deviations in Fig. 11(b), the angle φ_{ac} keeps a good tolerance and nearly stabilizes within the range of 25.0°~25.5°, while φ_{AC} slightly reduces after the two-stage transformations, which well verifies the theoretical analysis in Section III. By tinily reducing either the transmitter capacitor or the switching frequency, these derivatives of impedances and phases can be readily alleviated and flexibly utilized for realizing the robust ZVS. A switching phase angle can be

stabilized for maintaining the ZVS, thus inherently withstanding both the varying loads and mutual inductances. Whereas in the SS-WPT with only one-stage transformation, a varying phase φ_{AC}, by which $\mathbf{U}_{AC}$ lags $\mathbf{I}_t$, will be generated with a rectification-caused and converted virtual capacitance, which deteriorates the ZVS, thus degrading the system performance.

Figs. 12(a) and 12(b) show the theoretical system efficiencies of proposed high-order transformation scheme versus the different loads and mutual inductances, respectively. By adding a high-order *LCC*-transformation, the robust ZVS can readily be realized in the proposed system even operating in a boost mode. For the investigated scenarios of battery trickle charging and LED dimming, since the equivalent load will gradually increase, the system efficiency will monotonously increase and finally stabilize at a maximum value of 93.25% with an increasing load and a fixed 5.0-μH mutual inductance. At a fixed load of 400 Ω, this efficiency will also monotonously increase with the increasing mutual inductance and reach up to 95.01%.

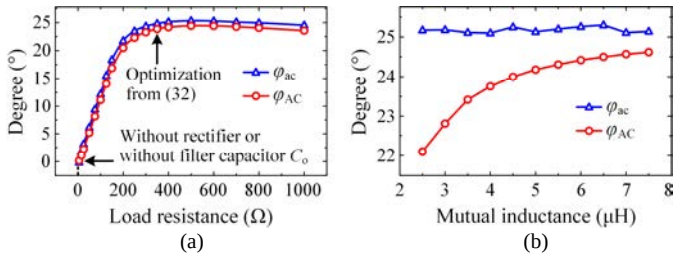

Fig. 11. Phase characteristics of two-stage high-order *LCC*-transformation scheme. (a) With varying loads. (b) With varying mutual inductances.

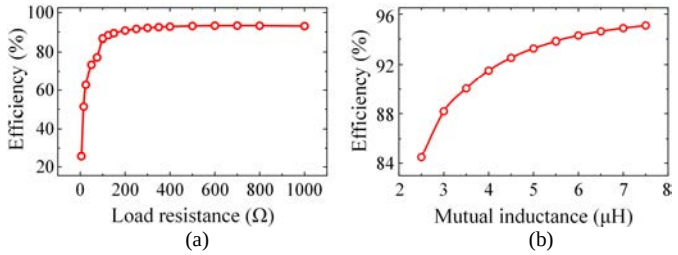

Fig. 12. System efficiencies of proposed high-order *LCC*-transformed HFP-WPT system. (a) With different loads. (b) With different mutual inductances.

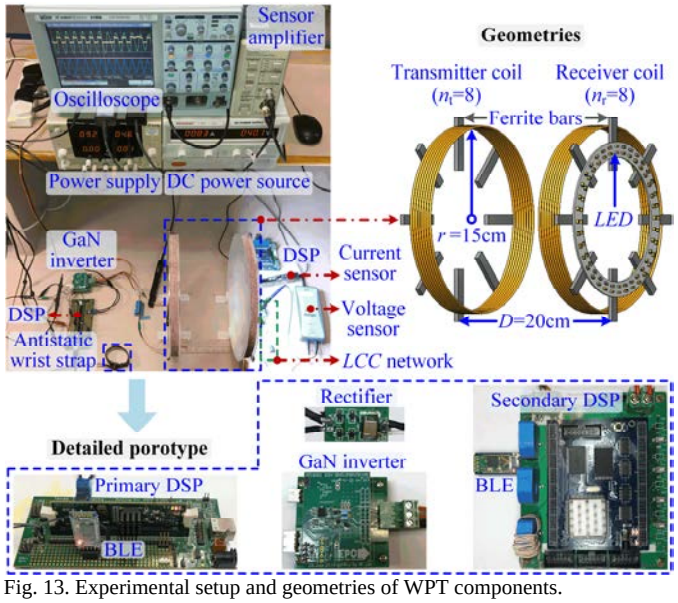

Fig. 13. Experimental setup and geometries of WPT components.

V. Experimental Verifications

To verify the feasibility of proposed high-order *LCC*-transformed WPT using the ZVS-HFP technique, a prototype using an *LCC*-transformation was constructed and the relevant experimentation was performed for demonstration in Fig. 13, where both the 3-D geometries of WPT components and the detailed prototype are also illustrated. The design specifications of prototype are listed in Table II, where the estimated dissipation factor is 0.06% at 600 kHz. The coil AC resistances are also listed. The inverter is populated with the enhancement mode gallium nitride (eGaN) field-effect transistors (FETs) of EPC2010C. The specification of Litz wire is 250×0.10 mm.

TABLE II
Design Specifications and Parameters of the Prototype

Parameter	Symbol	Value
DC Input voltage	U_{in}	40~80 V
Maximum DC output voltage	U_o	120 V
Turns of transmitter and receiver coils	n_t, n_r	8
Coil outline radius	r_t, r_r	15 cm
Transmitter coil inductance	L_t	48.72 μH
Transmitter coil internal resistance	R_{Lt}	0.260 Ω
Transmitter compensated capacitance	C_t	1.435 nF
Transmitter capacitance ESR	R_{Ct}	0.111 Ω
Receiver coil inductance	L_r	45.60 μH
Receiver coil internal resistance	R_{Lr}	0.305 Ω
Receiver compensated capacitance	C_r	3.416 nF
Receiver capacitance ESR	R_{Cr}	0.047 Ω
Coupling coefficient	k	0.5-0.15
Receiver filter inductance	L_f	25.0 μH
Receiver filter internal resistance	R_{Lf}	0.293 Ω
Receiver filter capacitance	C_f	2.815 nF
Receiver filter capacitance ESR	R_{Cf}	0.057 Ω
DC filter capacitance	C_o	1 μF
Nominal resonant frequency	f	600 kHz
Capacitor dissipation factor @100 kHz	tanδ	0.04%
eGaN FETs	EPC2010C	-
Digital signal processer (DSP)	TMS320F28335	-
Measured maximum system efficiency	η	91.78%

A. Experimental Results

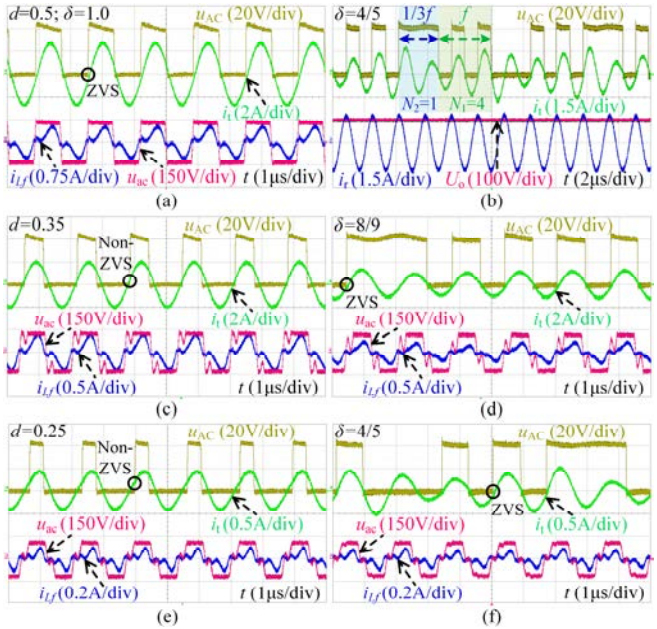

Fig. 14. Measured waveforms of high-order *LCC*-transformed boost WPT system. (a) d=0.5 (PWM) or δ=1.0 (HFP). (b) Insignificant output fluctuations. (c) d=0.35 (PWM). (d) δ=8/9 (HFP). (e) d=0.25 (PWM). (f) δ=4/5 (HFP).

Firstly, with different duty ratios d in the PWM and δ in the HFP, Fig. 14 shows the measured waveforms of the input voltage u_{AC}, transmitter current i_t, inductor current i_{Lf} and input voltage u_{ac} (before rectification) or output voltage U_o. It can be observed that the inputs (i_{Lf} and u_{ac}) before rectification are distorted in the boost WPT. By adding the high-order *LCC*-transformation to tactfully convert the phase derivatives, system optimization is realized by tinily reducing either the transmitter capacitor or the switching frequency so as to reliably enable the robust ZVS. Under the PWM, Figs. 14(a), 14(c) and 14(e) indicate that the ZVS will be deteriorated with a reducing duty ratio d, and thus the high-frequency hard-switching will cause more power and efficiency losses. Whereas under the HFP with a variable δ, Figs. 14(b), 14(d) and 14(f) show that the HFP input voltage can energize the transmitter current slightly before the zero-crossing points with a robust ZVS while maintaining the insignificant output fluctuations and the high system efficiency during power control. These measured results well confirm the oscillation frequency invariance, switching frequency suppression and robust ZVS operation, which well agrees with their theoretical analyses.

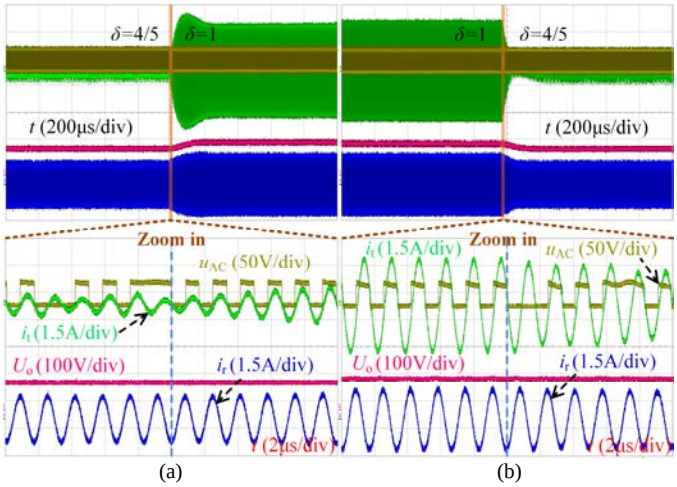

Fig. 15. Dynamic responses of proposed ZVS-HFP high-order *LCC*-transformed WPT system. (a) Increasing duty ratio. (b) Decreasing duty ratio.

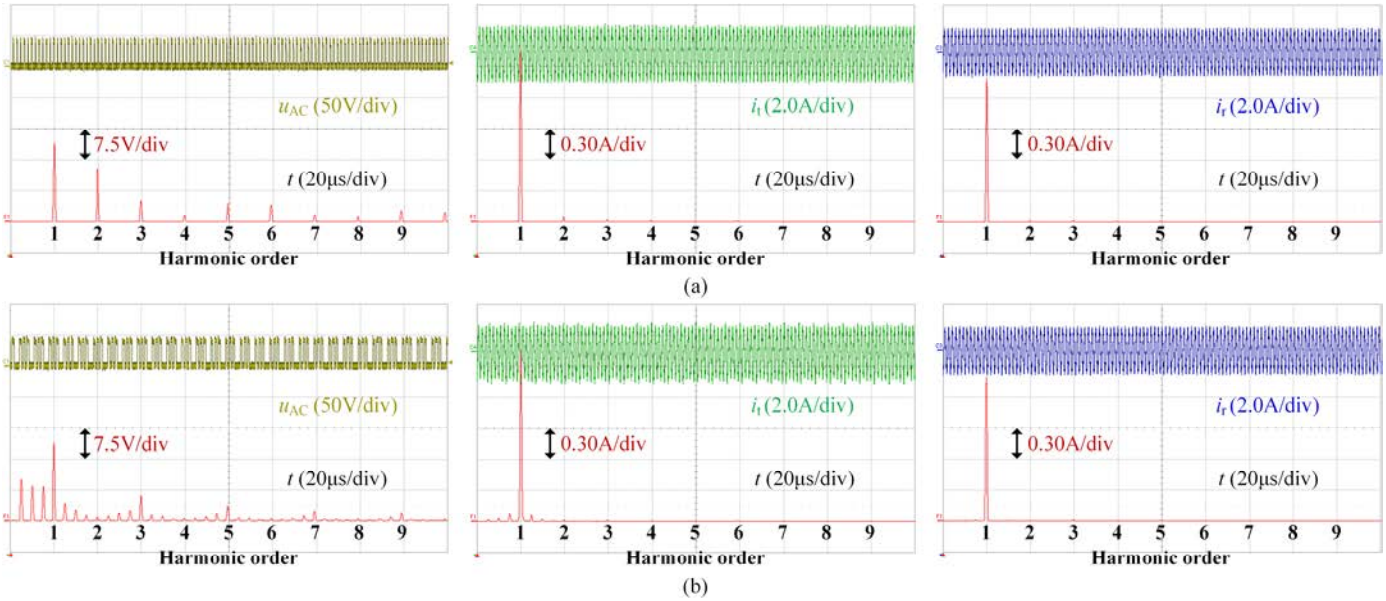

Fig. 16. Harmonic spectrums using FFT analysis. (a) PWM. (b) HFP.

Furthermore, during power control, Fig. 15 shows the dynamic responses and their zoom-in waveforms by using the proposed ZVS-HFP technique with a varying duty ratio δ. With an increasing δ from 4/5 to 1.0 in Fig. 15(a), the HFP is identified to dynamically energize the high-order *LCC*-transformed WPT with a robust ZVS. Also, minimizing the modulated numbers N_1 and N_2 can successfully enable the WPT system to output the insignificant fluctuations. Similarly, with a decreasing δ from 1.0 to 4/5 in Fig. 15(b), the HFP input voltage can flexibly power the WPT scheme with the ZVS and insignificant output fluctuations. Especially for dynamic power adjustment, the use of high-order *LCC*-transformation scheme, cooperating with the proposed HFP technique, can reliably realize the full-range robust ZVS via system optimization, thus readily getting rid of the requirement of complex ZVS phase control [16]. By using the FFT analysis, Figs. 16(a) and 16(b) show the harmonic spectrums of the inverter output u_{AC}, transmitter current i_t and receiver current i_r under the PWM and the HFP, respectively. In Fig. 16(a), the PWM produces the considerable even-order (2^{nd}, 4^{th}, 6^{th}, …) harmonics, especially in u_{AC}, while the HFP can significantly suppress the even-order harmonics but involves the inter-harmonics and subharmonics, especially near the switching frequency as shown in Fig. 16(b). As a result, the high-order (2^{nd}, 3^{rd}, 4^{th}, …) harmonics are reduced by using the HFP. Under two control methods, all the high-order harmonics, inter-harmonics and subharmonics are filtered to an insignificant level by the WPT resonant circuits. It well confirms the harmonic analysis in Section IV. Although the THDs of currents i_t and i_r are slightly higher due to the inter-harmonics and subharmonics, the HFP can realize a robust ZVS for power control.

Finally, by applying the PWM and the ZVS-HFP (n_f=1), respectively, Figs. 17(a) and 17(b) show the measured switching angles and output powers P_o versus their respective control objectives of d and δ, where $\delta_{AC,PWM,1}=\delta_{AC,HFP,1}$ from

(5) and (6). In Fig. 17(a), the switching angle φ_{AC} slightly increases under the HFP since the equivalent load increases with the decreasing δ. The high-order *LCC*-transformed WPT can always satisfy the minimum requirement of switching angle and operates stably within a ZVS region. Unfortunately, the decreasing d and pulse width will gradually lower the switching angle to become a negative value, which leads the PWM inverter to work within a non-ZVS region. Besides, in Fig. 17(b), two output powers monotonically decrease with the decreasing duty ratios, which well verifies the power control performance in Fig. 9(b). Fig. 17(c) shows the system efficiencies and duty ratios with respect to the varying percentage of output power. At 20-cm transfer distance, the high-order *LCC*-transformed WPT using two control methods works at the same system efficiency of 91.78% with the same initial ZVS. During power control, however, the high-order *LCC*-transformed WPT using the robust ZVS-HFP can achieve a higher system efficiency, by up to 7.3%, than that using the PWM. Also, it can be further improved with a lower transfer distance or at a larger power level. These results well confirm that the full-range robust ZVS-HFP technique can effectively reduce the power losses and thus improve the system efficiency. Consequently, the proposed ZVS-HFP is promising practically attractive for various WPT applications desiring wireless power control, such as battery charging management, motor speed control and LED dimming.

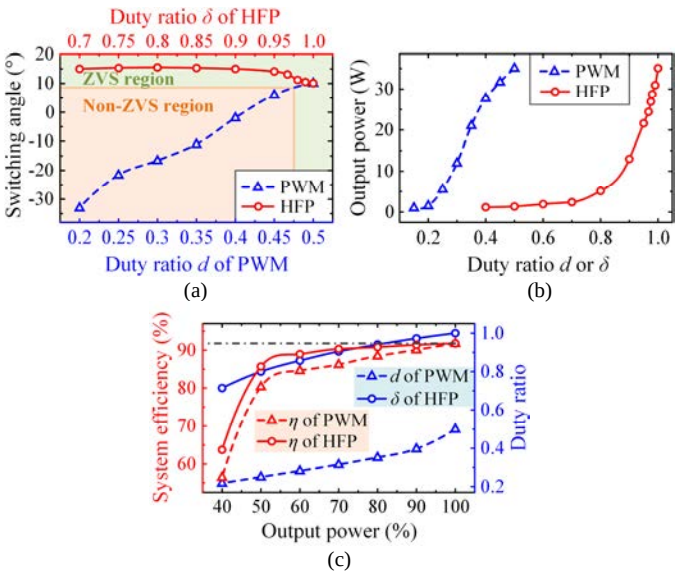

Fig. 17. Measured characteristics of proposed ZVS-HFP high-order *LCC*-transformed WPT system. (a) Switching phase angles. (b) Output powers. (c) System efficiencies and duty ratios.

B. Discussions and Recommendations

The input voltage of 40 V is adopted at the 20-cm transfer distance, which is compatible with the flexible battery-powered scenarios. For a larger coupling coefficient up to 0.15, it should be gradually increased to 80 V for achieving the same rated outputs. By designing parallel or series combinations, the exact capacitors can be made up of various specific capacitors picked up by using an LCR meter. Practically, the resonant frequency can be flexibly adjusted for selecting other readily available capacitors because the HFP is based on digital implementation. The loose coupling is to implement the WPT for a relatively long distance. Although the electromagnetic exposure is not easy to be shielded, the flux densities are very low for the exemplified low-power LED dimming. Without any shielding, the electromagnetic exposure may be insignificant with a very short safety distance. The proposed system can be promisingly used in the unguarded industrial or outdoor environments with good isolation, waterproof, sparkproof and flexibility. Significantly, the HFP and high-order transformation can be readily applied to the more tightly coupled scenarios with easy shielding for power control, such as domestic applications.

Under the PWM, the main part of inverter loss is due to the high-frequency hard-switching. Under the ZVS-HFP technique, the inverter switching loss is negligible. The HFP can significantly reduce the inverter loss in either the relatively low-frequency or high-frequency WPT applications in terms of wireless power control, especially improving the system efficiency for the high-frequency ones. The capacitance tolerance is usually ±5%. The HFP can achieve the reduced-frequency ZVS against the +5% capacitance tolerance during power control. With the –5% capacitance tolerance, the resonant frequency will slightly increase by 2.24%. The phase φ_{AC}, by which $\mathbf{U}_{AC}$ leads $\mathbf{I}_t$, will be lower and even probably become negative. Hence, both the PWM and the HFP may fail to maintain the ZVS except for optimizing the capacitors or the switching frequency. Significantly, considering the same capacitance tolerance, the HFP can still achieve a better system performance than the PWM can during power control. To avoid this influence, more precise capacitors can be used with ±2.5% capacitance tolerance which is available from industries. Besides, either the switching frequency or capacitor can be predesigned with a slight increase for realizing the frequency-reduced ZVS-HFP.

Since the ZVS-HFP technique is actually proceeding with the rhythm of transmitter resonance, it can be extended to any WPT topologies using series/parallel, high-order T-circuits and their higher-order combination networks, so long as the transmitter resonates stably. These topologies can enable the WPT system to achieve both the load-independent outputs [21] and the desired transfer ratio [22]. It should be noted that there are no requirements and limitations for receiver topologies but few ones for transmitter: 1) Parallel compensation is not suitable to be powered by voltage-source inverters; 2) If the high-order or higher-order T-circuits are used, only the first T-circuit after the inverter should be tuned to form the required resonance in [22], and all other T-circuits can be flexibly tuned according to [20] and [22]; 3) Switching frequency deviation should be taken for both the HFP and the PWM to cope with the frequency bifurcation. On the other hand, the HFP can effectively eliminate the even-order harmonics during power control compared with the PWM (d<0.5) but at the expense of slightly adding the inter-harmonics and subharmonics near the switching frequency. Hence, the transmitter current will slightly fluctuate, while the receiver fluctuations are insignificant. The bandwidth of control loop will be low and mainly restricted by the connection interval of wireless communication [26], but the control system can keep stable with the required phase and gain margins withstanding a load step. Also, the ZVS-HFP modulation will not increase the possibility of system instability as compared with the PWM.

VI. Conclusion

In this paper, an HFP technique and a high-order *LCC* transformation have been proposed and then implemented for tuning a high-efficiency WPT system with a robust ZVS. By pacing the electromagnetic resonances for hybrid-frequency energized WPT, the proposed HFP technique can readily realize the reduced-frequency ZVS so as to improve the system efficiency as compared with the PWM. For various boost WPT scenarios with rectification-caused load-dependent derivatives, a high-order *LCC*-transformation is newly explored and identified to flexibly convert and utilize these very low virtual derivatives, which can offer the required switching angle for maintaining a robust ZVS-HFP. The experimental system efficiency can be over 91.5% and improved by up to 7.3% during power control with the full-range robust ZVS operation. Both theoretical analysis and hardware experimentation are given to verify the feasibility of proposed HFP technique for tuning the high-order *LCC*-transformed WPT system.

References

[1] G. A. Covic and J. T. Boys, "Inductive power transfer," *Proc. IEEE*, vol. 101, no. 6, pp. 1276–1289, Jun. 2013.

[2] Z. Zhang, H. Pang, A. Georgiadis and C. Cecati, "Wireless power transfer – an overview," *IEEE Trans. Ind. Electron.*, vol. 66, no. 2, pp. 1044–1058, Feb. 2019.

[3] C. C. Mi, G. Buja, S. Y. Choi and C. T. Rim, "Modern advances in wireless power transfer systems for roadway powered electric vehicles," *IEEE Trans. Ind. Electron.*, vol. 63, no. 10, pp. 6533–6545, Oct. 2016.

[4] X. Dai, J. Jiang and J. Wu, "Charging area determining and power enhancement method for multiexcitation unit configuration of wirelessly dynamic charging EV system," *IEEE Trans. Ind. Electron.*, vol. 66, no. 5, pp. 4086–4096, May 2019.

[5] C. Jiang, K. T. Chau, W. Liu, C. Liu, W. Han, and W. H. Lam, "An LCC compensated multiple-frequency wireless motor system," *IEEE Trans. Ind. Inform.*, vol. 15, no. 11, pp. 6023–6034, Nov. 2019.

[6] Y. Li et al., "Analysis, design and experimental verification of a mixed high order compensations-based WPT system with constant current outputs for driving multistring LEDs," *IEEE Trans. Ind. Electron.*, vol. 67, no. 1, pp. 203–213, Jan. 2020.

[7] W. Liu, K. T. Chau, C. H. T. Lee, C. Jiang, W. Han and W. H. Lam, "Wireless energy-on-demand using magnetic quasi-resonant coupling", *IEEE Trans. Power Electron.*, vol. 35, no. 9, pp. 9057-9069, Sep. 2020.

[8] Z. Zhang, K. T. Chau, C. Qiu, and C. Liu, "Energy encryption for wireless power transfer," *IEEE Trans. Power Electron.*, vol. 30, no. 9, pp. 5237–5246, Sep. 2015

[9] Y. Chen et al., "Variable-parameter T-circuit-based IPT system charging battery with constant current or constant voltage output," *IEEE Trans. Power Electron.*, vol. 35, no. 2, pp. 1672–1684, Feb. 2020.

[10] W. Han, K. T. Chau, C. Jiang, W. Liu and W. H. Lam, "High-order compensated wireless power transfer for dimmable metal halide lamps," *IEEE Trans. Power Electron.*, vol. 35, no. 6, pp. 6269–6279, Jun. 2020.

[11] Y. Fang, B. M. H. Pong and S. Y. R. Hui, "An enhanced multiple harmonics analysis method for wireless power transfer systems," *IEEE Trans. Power Electron.*, vol. 35, no. 2, pp. 1205–1216, Feb. 2020.

[12] F. Chen, H. Garnier, Q. Deng, M. K. Kazimierczuk and X. Zhuan, "Control-oriented modeling of wireless power transfer systems with phase-shift control," *IEEE Trans. Power Electron.*, vol. 35, no. 2, pp. 2119–2134, Feb. 2020.

[13] H. Li, K. Wang, J. Fang and Y. Tang, "Pulse density modulated ZVS full-bridge converters for wireless power transfer systems," *IEEE Trans. Power Electron.*, vol. 34, no. 1, pp. 369–377, Jan. 2019.

[14] W. Liu, K. T. Chau, C. H. T. Lee, W. Han, X. Tian and W. H. Lam, "Full-range soft-switching pulse frequency modulated wireless power transfer", *IEEE Trans. Power Electron.*, vol. 35, no. 6, pp. 6533–6547, Jun. 2020.

[15] S. Ryu, D. Kim, M. Kim, J. Kim and B. Lee, "Adjustable frequency-duty-cycle hybrid control strategy for full-bridge series resonant converters in electric vehicle chargers," *IEEE Trans. Ind. Electron.*, vol. 61, no. 10, pp. 5354–5362, Oct. 2014.

[16] Y. Jiang, L. Wang, Y. Wang, J. Liu, X. Li and G. Ning, "Analysis, design, and implementation of accurate ZVS angle control for EV battery charging in wireless high-power transfer," *IEEE Trans. Ind. Electron.*, vol. 66, no. 5, pp. 4075–4085, May 2019.

[17] J. M. Rivas, O. Leitermann, Y. Han and D. J. Perreault, "A very high frequency DC-DC converter based on a class Φ_2 resonant inverter," *IEEE Trans. Power Electron.*, vol. 26, no. 10, pp. 2980–2992, Oct. 2011.

[18] J. M. Rivas, Y. Han, O. Leitermann, A. D. Sagneri and D. J. Perreault, "A high-frequency resonant inverter topology with low-voltage stress," *IEEE Trans. Power Electron.*, vol. 23, no. 4, pp. 1759–1771, Jul. 2008.

[19] J. Hu, A. D. Sagneri, J. M. Rivas, Y. Han, S. M. Davis and D. J. Perreault, "High-frequency resonant SEPIC converter with wide input and output voltage ranges," *IEEE Trans. Power Electron.*, vol. 27, no. 1, pp. 189–200, Jan. 2012.

[20] S. Li, W. Li, J. Deng, T. D. Nguyen, and C. C. Mi, "A double-sided LCC compensation network and its tuning method for wireless power transfer," *IEEE Trans. Veh. Technol.*, vol. 64, no. 6, pp. 2261–2273, Jun. 2015.

[21] X. Qu, Y. Jing, H. Han, S. Wong and C. K. Tse, "Higher order compensation for inductive-power-transfer converters with constant-voltage or constant-current output combating transformer parameter constraints," *IEEE Trans. Power Electron.*, vol. 32, no. 1, pp. 394–405, Jan. 2017.

[22] J. Lu, G. Zhu, D. Lin, S. Wong and J. Jiang, "Load-independent voltage and current transfer characteristics of high-order resonant network in IPT system," *IEEE J. Emerg. Sel. Topics Power Electron.*, vol. 7, no. 1, pp. 422–436, Mar. 2019.

[23] Y. Xiao, C. Liu, Y. Huang and S. Liu, "Concurrent wireless power transfer to multiple receivers with additional resonant frequencies and reduced power switches," *IEEE Trans. Ind. Electron.*, doi: 10.1109/TIE.2019.2952787.

[24] W. Liu, K. T. Chau, C. H. T. Lee, C. Jiang, W. Han and W. H. Lam, "Multi-frequency multi-power one-to-many wireless power transfer system," *IEEE Trans. Magn.*, vol. 55, no. 7, pp. 1–9, Jul. 2019.

[25] X. Zhang, T. Kan, C. You and C. C. Mi, "Modeling and analysis of AC output power factor for wireless chargers in electric vehicles," *IEEE Trans. Power Electron.*, vol. 32, no. 2, pp. 1481–1492, Feb. 2017.

[26] T. Tan, K. Chen, Y. Jiang, Q. Lin, L. Yuan and Z. Zhao, "A bidirectional wireless power transfer system control strategy independent of real-time wireless communication," *IEEE Trans. Ind. Appl.*, vol. 56, no. 2, pp. 1587–1598, Mar. –Apr. 2020.

Wei Liu (S'17) received the B.Eng. degree in electrical engineering and automation and the M.Eng. degree in electrical engineering from China University of Petroleum (East China), Qingdao, China, in 2014 and 2017, respectively. He is currently working toward the Ph.D. degree in electrical and electronic engineering at the Department of Electrical and Electronic Engineering, The University of Hong Kong, Hong Kong.

He was a Visiting Researcher with the Nanyang Technological University, Singapore, in 2019. His research interests include power electronics, wireless power transfer techniques, and electric vehicle technologies.

K. T. Chau (M'89–SM'04–F'13) received the B.Sc. (Eng.), M.Phil., and Ph.D. degrees in electrical and electronic engineering from The University of Hong Kong, Hong Kong, in 1988, 1991, and 1993, respectively.

Since 1995, he has been with The University of Hong Kong, where he is currently a Professor in the Department of Electrical and Electronic Engineering. He is the author of nine books and more than 300 journal papers. His research interests include electric and hybrid vehicles, power electronics and drives, and renewable energies.

Prof. Chau is a Fellow of the Institution of Engineering and Technology (IET), U.K., and of the Hong Kong Institution of Engineers. He is currently also a Co-editor of the *Journal of Asian Electric Vehicles*. He is a Chartered Engineer in Hong Kong. He was the recipient of the Changjiang Chair Professorship from the Ministry of Education, China, and the Environmental Excellence in Transportation Award for Education, Training, and Public Awareness from the Society of Automotive Engineers International.

Christopher H. T. Lee (M'12–SM'18) received the B.Eng. (First Class Hons.) and Ph.D. degrees in electrical engineering from Department of Electrical and Electronic Engineering, The University of Hong Kong, Hong Kong, in 2009 and 2016, respectively.

He is currently an Assistant Professor in power engineering with the Nanyang Technological University, Singapore, a Visiting Assistant Professor with the Massachusetts Institute of Technology, Cambridge, MA, USA, and an Honorary Assistant Professor in the *alma mater*. His research interests are Electric Machines and Drives, Renewable Energies, and Electric Vehicle Technologies. In these areas, he has published 1 book, 3 book chapters, and about 70 referred papers.

Dr. Lee was recipient of many awards, including the Li Ka Shing Prize (the best Ph.D. thesis prize) and the Croucher Foundation Fellowship to support his postdoctoral research.

Xiaoyang Tian (S'18) received the B.Eng. in electrical engineering and automation from Hangzhou Dianzi University, Hangzhou, China, in 2015, and the M.Eng. degrees in electrical engineering from North China Electric Power University, Baoding, China in 2018. He is currently working toward the Ph.D. degree in electrical and electronic engineering at the Department of Electrical and Electronic Engineering, The University of Hong Kong, Hong Kong, China.

His research interests include wireless power transfer techniques, power electronics, and electric vehicle technologies.

Chaoqiang Jiang (S'16–M'19) received the B.Eng. and M.Eng. degrees in automation from Wuhan University, Wuhan, China, in 2012 and 2015, respectively, and the Ph.D. degree in electrical and electronic engineering from The University of Hong Kong, Hong Kong, in 2019.

He is currently a Postdoctoral Research Associate with the University of Cambridge, U.K. In 2019, he was a Visiting Researcher with the Nanyang Technological University, Singapore. His research interests include power electronics, wireless power transfer techniques, and electric vehicle technologies.